ROYAL SOCIETY
OF CHEMISTRY

Check for updates

Optimizing d–p orbital hybridization by tuning high-entropy spinel oxides for enhanced alkaline OER efficiency†

Dongyuan Song, [ID] [a] Xueda Liu, [ID] [a] Yingkai Wu, [a] Quan Quan, [b] Yuta Tsuji, [ID] [c]
Xiaoge Liu, [a] Hikaru Saito, [d] Shiro Ihara, [ID] [d] Liyuan Dai, [a] Xiaoguang Liang, [ID] [ef]
Takeshi Yanagida, [dg] Johnny C. Ho [ID] *[bdh] and SenPo Yip*[d]

The growing need for cost-effective and efficient energy conversion technologies drives the development of advanced catalysts for the oxygen evolution reaction (OER). Our research focuses on high-entropy spinel oxides (HESOs) as efficient OER electrocatalysts. Using the molten salt synthesis (MSS) method, we prepared HESO nanoparticles from Fe, Ni, Co, Mn, and Zn. By adjusting the precursor ratios, we obtained equimolar $(Ni_{0.2}Fe_{0.2}Co_{0.2}Mn_{0.2}Zn_{0.2})_3O_4$, CoMn-rich, and NiFe-rich samples to examine compositional effects. Among these, the CoMn-rich HESO sample exhibited superior catalytic performance in 1 M KOH solution, with an overpotential of 330.1 mV at 10 mA cm^{-2} and a Tafel slope of 53.5 mV dec^{-1}. Its promising long-term stability and enhanced reaction kinetics are significant. The synergistic effect of Co and Mn with high valence states and enhanced oxygen adsorption on the CoMn-rich HESO lower the energy barrier and accelerate electron transfer, improving the reaction kinetics. Density functional theory (DFT) calculations further reveal the relationship between orbital hybridization and catalytic performance, emphasizing the contribution of high valence metal active centers in improving performance. The density of states (DOS) analysis further demonstrates the stronger covalency between the 3d orbitals of the metal active site and the O 2p orbitals on the surface of CoMn-rich samples, which favors the absorption of oxygen species and thus improves the electrochemical performance. This work presents an effective method for HESO synthesis and opens new avenues for energy conversion research.

1. Introduction

Hydrogen is widely considered a promising green fuel with high energy density that can help address the energy crisis and mitigate the adverse environmental impacts of fossil fuel utilization.[1–5] Water electrolysis is an attractive approach to

[a]Interdisciplinary Graduate School of Engineering Sciences, Kyushu University, Fukuoka 816-8580, Japan

[b]Department of Materials Science and Engineering, City University of Hong Kong, Hong Kong SAR 999077, P. R. China. E-mail: johnnyho@cityu.edu.hk

[c]Faculty of Engineering Sciences, Kyushu University, Fukuoka 816-8580, Japan

[d]Institute for Materials Chemistry and Engineering, Kyushu University, Fukuoka 816-8580, Japan. E-mail: yip.sen.po.472@m.kyushu-u.ac.jp

[e]School of Physical Science and Technology, Guangxi Normal University, Guilin 541004, P. R. China

[f]Guangxi Key Laboratory of Low Carbon Energy Materials, Guangxi Normal University, Guilin, 541001, P. R. China

[g]Department of Applied Chemistry, Graduate School of Engineering, The University of Tokyo, Tokyo 113-8656, Japan

[h]State Key Laboratory of Terahertz and Millimeter Waves, City University of Hong Kong, Hong Kong SAR 999077, P. R. China

† Electronic supplementary information (ESI) available. See DOI: https://doi.org/10.1039/d4ta08485c

economically and environmentally friendly hydrogen production.[4,6] In recent years, advancements in water splitting have predominantly concentrated on addressing the sluggish kinetics of the oxygen evolution reaction (OER).[7,8] While noble metal electrocatalysts like RuO_2 and IrO_2 are highly effective for OER, their high cost and limited availability pose significant barriers to widespread adoption.[9–12] Consequently, there is growing interest in developing transition metal-based catalysts (Ni, Fe, Co, *etc.*), which are more affordable, abundant, and offer a promising alternative to noble metal-based electrocatalysts.[13–15] Toward this end, developing highly active and durable electrocatalysts based on 3d transition metal oxides for OER in alkaline media is essential to enhance water-splitting efficiency and cost-effectiveness.

High-entropy alloys (HEAs) were initially introduced by Yeh *et al.* in 2004.[16] Since then, various high-entropy materials (HEMs) with high configurational entropy and containing five or more metal cations within a solid solution,[17] have gained considerable attention for applications in catalysis,[18–20] fuel cell,[21,22] and energy storage.[23,24] Compared to traditional low-entropy catalysts, HEMs offer multi-element synergistic interactions and structural complexity, providing diverse, active sites and optimizing electronic configurations to enhance catalytic

This journal is © The Royal Society of Chemistry 2025

J. Mater. Chem. A, 2025, **13**, 13295–13304 | 13295

performance and stability. Additionally, their tailorable composition allows for developing high-performance, low-cost catalysts using abundant elements.[25–27] Based on this design strategy, high-entropy oxides (HEOs) have particularly emerged as OER catalysts to improve the catalytic performance by carefully tuning the compositions.[18,28,29] For example, Zhang et al.[30] observed that the entropy-engineered $(CoNiMnZnFe)_3O_{3.2}$ showed an overpotential of 336 mV at a current density of 10 mA cm^{-2}, which is significantly lower than its low-entropy counterparts. In another report, Wang et al.[31] studied the OER activity of HEO nanoparticles, which were synthesized using a low-temperature solvothermal method, exhibiting an overpotential of 350 mV at 10 mA cm^{-2} in alkaline environment. Nguyen et al.[32] investigated La-based perovskite HEOs, including diverse B site cations such as Cr, Mn, Fe, Co, and Ni, achieving a 325 mV overpotential at 10 mA cm^{-2}. This value is significantly lower than that of low-entropy counterparts, demonstrating that electrochemical performance can be optimized by tuning the composition.

High-entropy compounds can theoretically form from all metal atoms due to entropy increase at high temperatures, as described by the Gibbs free energy equation ($\Delta G_{mix} = \Delta H_{mix} - T\Delta S_{mix}$).[33] However, several factors are hindering the stability of high-entropy materials, such as the effect of atomic radius differences on different crystalline structures,[34] phase transitions,[35] and high-temperature stability. Most synthetic methods for HEOs require high temperatures (≥ 900 °C), so it is not easy to synthesize stable HEOs.[36] In order to achieve structural stabilization of high-entropy compound systems, a novel design approach is highly desirable. It may give a unique opportunity for further research into HEMs. In particular, the molten salt synthesis (MSS) method is a green, efficient, cost-effective, sustainable, versatile, and generalizable technique for synthesizing nanomaterials.[37,38] The two key advantages of MSS that distinguish it from other techniques are its ability to lower the product formation temperature and its effectiveness in producing uniform particles.[38–41] Various reports have then demonstrated the synthesis of HEOs using the MSS method. For instance, Xue et al.[42] synthesized a phase-pure rock salt-type HEO by MSS, which was introduced as an anode material for lithium-ion batteries with high specific capacity and cycling stability.

In this work, we employed a one-step MSS method to prepare equimolar $((Ni_{0.2}Fe_{0.2}Co_{0.2}Mn_{0.2}Zn_{0.2})_3O_4)$ and non-equimolar (CoMn-rich and NiFe-rich) high-entropy spinel oxides (HESOs) nanoparticles by controlling the ratio of each element in the precursor for efficient and durable OER. The molten salt medium acts as an ionic liquid, with its strong polarization enabling the dissolution of most transition metal oxides. Thus, this dissolution process allows for tuning the compositions of the as-synthesized products. The obtained CoMn-rich HESO exhibits enhanced catalytic performance in 1 M KOH solution with an overpotential of 330.1 mV at 10 mA cm^{-2}, a small Tafel slope of 53.5 mV dec^{-1}, and no apparent degradation for 120 hours. After careful characterization, it was found that the change in composition significantly impacted the amount of high-valance transition metal ions and the adsorption ability of

oxygen species, thereby affecting the OER performance. DFT calculations reveal that optimizing d–p coupling through composition engineering promotes the redistribution of surface electrons and influences the surface free energy of adsorbed intermediates, thereby enhancing electrocatalytic performance. This work presents a viable approach to designing HESOs by engineering their composition, offering a new strategy for optimizing their performance in the OER.

2. Experimental

2.1 Chemicals and materials

Fe_2O_3 (99.9%), NiO (99.9%), MnO_2 (99.5%), ZnO (99%), NaCl (99.5%), KCl (99.5%), KOH (85%) and Nafion (5 wt%) were purchased from Wako, Japan. CoO and RuO_2 (99.9%) were provided by Sigma-Aldrich. Carbon black Vulcan XC-72R was purchased from Fuel Cell Earth. The Hg/HgO and glassy carbon (GC) electrodes were obtained from ALS Co., Ltd, Japan.

2.2 Synthesis of high entropy oxide nanoparticles

The equimolar, CoMn-rich, and NiFe-rich HESO nanoparticles were synthesized from oxide powders using the MSS method. 0.5 g of metal oxides were weighed according to the stoichiometric number and mixed with 5 g of NaCl and KCl in a molar ratio of 1 to 1. The mixture was ball-milled at room temperature for 4 hours at 350 rpm. After ball milling, the powder mixture was placed in an Al_2O_3 crucible and then calcined at 750 °C for 2 hours in a muffle furnace. The crucible was allowed to cool to room temperature. Next, the as-prepared product was collected and thoroughly washed with deionized water to eliminate residual NaCl and KCl. After washing, the remaining product was collected for further structure characterization and electrocatalytic analysis after being dried in an oven at 60 °C for 12 hours. As a control experiment, $(Ni_{0.5}Fe_{0.5})_3O_4$, $(Ni_{0.33}Fe_{0.33}Co_{0.33})_3O_4$, and $(Ni_{0.25}Fe_{0.25}Co_{0.25}Mn_{0.25})_3O_4$ were also prepared by using a similar process.

2.3 Characterizations of electrocatalysts

Scanning electron microscope (SEM, Thermo Fisher Scientific Helios Hydra CX working at 10 kV) and energy-dispersive spectrometry (EDS, Oxford instruments Xplore) were used to investigate the samples' morphology and composition. The composition of samples was also determined using an Agilent 7900 inductively coupled plasma mass spectrometer (ICP-MS). Scanning transmission electron microscopy (STEM) operating at 300 kV, equipped with a four-quadrant windowless Super-X silicon drift detector and energy-dispersive X-ray spectroscopy (EDS), was performed on a Titan Cubed G2 microscope from Thermo Fisher Scientific to characterize the microstructure and elemental distribution. The X-ray powder diffractor (XRD, Rigaku RINT-TTRIII) with Cu Kα radiation source ($\lambda = 1.5418$ Å) was used to confirm the crystal structure of the as-prepared HESOs. X-ray photoelectron spectroscopy (XPS) was measured using Shimadzu/KRATOS Corporation AXIS-165 equipment for the valence states of each element in the as-synthesized catalysts.

13296 | J. Mater. Chem. A, 2025, **13**, 13295–13304

This journal is © The Royal Society of Chemistry 2025

2.4 Electrochemical measurements

All electrochemical measurements were conducted in a standard three-electrode system. A graphite rod with a diameter of 6 mm was used as the counter electrode. A standard Hg/HgO electrode was applied as the reference electrode, and a GC electrode with a diameter of 3 mm was employed as the working electrode. All electrodes were connected to an electrochemical workstation (Gamry 1010E, USA). For the preparation of the working electrode, 5 mg of the as-prepared product and 1 mg of carbon black was dispersed in a solution containing 255 μL of ethanol, 85 μL of deionized water, and 60 μL of Nafion (5 wt%) by sonication. 2 μL of the homogeneous solution was dropped onto the surface of GC with the mass loading 357.1 μg cm^{-2} and dried at room temperature. All of the electrochemical measurements were employed in 1 M oxygen-saturated KOH solution. The linear sweep voltammetry (LSV) curves were obtained at a scan rate of 10 mV s^{-1} from 0.2 to 0.8 V vs. Hg/HgO and were calibrated with IR compensation in the electrochemical workstation. All the measured potentials were converted to the potentials vs. reversible hydrogen electrode (RHE) using the following equation:
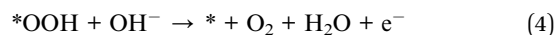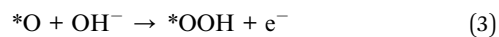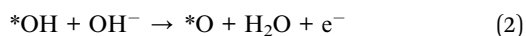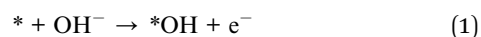
$$E_{RHE} = E_{Hg/HgO} + 0.059 \times pH + 0.098 \text{ V}$$

Electrochemical impedance spectroscopy (EIS) was performed at 330.1 mV vs. RHE throughout a frequency range of 100 kHz to 0.01 Hz. The electrical double-layer capacitance (C_{dl}) was assessed using cyclic voltammetry (CV) measurements in the non-faradic region, specifically between 1.04 and 1.14 V vs. RHE. CV measurements were taken at scan rates ranging from 20 to 100 mV s^{-1}. Moreover, the Tafel slope was achieved from the corresponding LSV data using the equation, $\eta = b \times \log(j)$, where η denotes the overpotential, b is the Tafel slope, and j is the current density. The stability of the electrocatalysts was measured using the chronopotentiometry (CP) method at 10 mA cm^{-2}, with 1 cm^2 of carbon cloth coated with 20 μL of electrocatalyst solution as the working electrode. The OER faradaic efficiency (FE) was determined by comparing experimental and theoretical O$_2$ quantities in a two-electrode cell utilizing a 1 M KOH electrolyte. The setup employed an H-shaped electrolytic cell with CoMn-rich HESOs as the cathode and a graphite rod as the anode. The gas collection was achieved using a simple drainage method. CP was conducted at a current of 10 mA to generate hydrogen and oxygen continuously. The FE calculation utilized the equation: FE = ZnF/Q, where Z represents the electron transfer count during water splitting ($Z = 4$ for OER), n denotes moles of oxygen produced, F is Faraday's constant (96 485 C mol^{-1}), and Q is the elementary electrode charge. This methodology allows for precise quantification of the OER efficiency in the electrochemical system. The turnover frequency (TOF) is calculated by the equation: TOF = $jA/4Fn$, where j is the current density at the overpotential of 400 mV, A represents the geometric surface area of the GC, F is Faraday's constant, n denotes moles of the active materials loaded on the GC, as measured by the ICP-MS.

2.5 DFT calculations

All first-principles calculations of (Fe$_x$Ni$_y$Co$_z$Mn$_v$Zn$_w$)$_3$O$_4$ (space group: $Fd\bar{3}m$) were performed using version 5.4.4 of the Vienna *ab initio* simulation package (VASP)[43,44] with Perdew–Burke–Ernzerhof (PBE)[45] to compare the activity of each electrocatalyst. The surface of (Fe$_x$Ni$_y$Co$_z$Mn$_v$Zn$_w$)$_3$O$_4$ was modeled with a slab thickness of 8 Å, and we utilized a 15 Å thick vacuum to avoid periodic image interactions. The direction corrected by dipole correction corresponds to the direction of the third lattice vector, the c-axis direction. The convergence criterion for the electronic self-consistent field loop was set to 1.0×10^{-8} eV. The atomic positions were fully optimized until the forces on all the atoms became less than 0.03 eV Å^{-1}. The DFT+U was employed, where U values are 4.6, 5.1, 5.0, 4.0, and 7.5 for Fe, Ni, Co, Mn, and Zn, respectively.[46] The cutoff energy was set to 500 eV, and the k-point meshes with a k spacing of $2\pi \times 0.05$ Å^{-1}. The pseudopotential is set with the projector augmented wave (PAW).[47] Grimme's D3 dispersion correction formalism with Becke–Johnson damping was adopted.[48]

The oxygen evolution reaction process in an alkaline environment can be broken down into the following four single-electron steps:

$$* + OH^- \rightarrow *OH + e^- \tag{1}$$

$$*OH + OH^- \rightarrow *O + H_2O + e^- \tag{2}$$

$$*O + OH^- \rightarrow *OOH + e^- \tag{3}$$

$$*OOH + OH^- \rightarrow * + O_2 + H_2O + e^- \tag{4}$$

where * represents active species on the catalyst surface and *OH, *O, and *OOH denote the adsorbed species at different steps, respectively.

The Gibbs free energy corresponding to the four steps above can be obtained according to the following equation:

$$\Delta G_1 = E_{*OH} - E_{H_2O} + \frac{1}{2}E_{H_2} + (\Delta ZPE - T\Delta S)_1 - eU_{RHE}$$

$$\Delta G_2 = E_{*O} - E_{*OH} + \frac{1}{2}E_{H_2} + (\Delta ZPE - T\Delta S)_2 - eU_{RHE}$$

$$\Delta G_3 = E_{*OOH} - E_{*O} - E_{H_2O} + \frac{1}{2}E_{H_2} + (\Delta ZPE - T\Delta S)_3 - eU_{RHE}$$

$$\Delta G_4 = E_* - E_{*OOH} + \left(2E_{H_2O} - \frac{3}{2}E_{H_2}\right) + \Delta G_0 \\ - (\Delta ZPE - T\Delta S)_4 - eU_{RHE}$$

where, E_{*OH}, E_{*O}, and E_{*OOH} are the adsorption energy of *OH, *O, *OOH, respectively. E_{H_2} and E_{H_2O} were obtained from the DFT calculations for the H$_2$ and H$_2$O molecules. The zero-point energy correction term (ΔZPE) can be calculated from vibrational frequency; T is temperature, and ΔS denotes the entropy change. $(\Delta ZPE - T\Delta S)_n$ ($n = 1, 2, 3, 4$) corresponds to the

This journal is © The Royal Society of Chemistry 2025

J. Mater. Chem. A, 2025, **13**, 13295–13304 | **13297**

thermal correction for each step, and its calculation details can be found elsewhere.[49] ΔG_0 is the free energy difference for the overall water oxidation reaction, which is 4.92 eV at $p = 1$ bar and $T = 298.15$ K. U_{RHE} is the potential of the electrode relative to the RHE. As is evident from the above equations, U_{RHE} equally affects all steps. Additionally, we confirmed, using thermal correction values obtained from the literature,[50] that the application or non-application of these values does not affect which step becomes the rate-determining step. Therefore, in this manuscript, these contributions are neglected for simplicity.

3. Results and discussion

A one-step MSS method was used to prepare the HESO nanoparticles. Fig. 1 illustrates the schematic representation of the synthetic procedures. NaCl and KCl eutectic mixtures were chosen as the molten salt because of their low cost, non-participation in reactions, and ease of removal. The mixture of precursors containing Fe, Ni, Co, Mn, Zn, and salts was first mixed thoroughly *via* ball milling. After that, the powder mixture was calcined to melt the eutectic salt mixture, facilitating the dissolution of precursors. As a result, the HESO particles began to nucleate and were successfully obtained.

The *ex situ* temperature-dependent XRD patterns are shown in Fig. 2a to analyze the phase transition of the equimolar HESO during the growth process. Comparing the XRD spectra at 400 °C and 600 °C, the sample exhibits multiple phases, with none being dominant. These results suggest that only minimal phase transitions occur within this temperature range, and a complete transition cannot be achieved. The major transformation began between 650 °C and 700 °C, around the melting point of the NaCl–KCl eutectic mixture. As indicated in Fig. 2a, five main diffraction peaks can be observed around 30.36°, 35.76°, 43.47°, 57.51° and 63.17° when the calcination temperature was over 700 °C, suggesting that these samples possessed a well-defined cubic spinel phase (space group $Fd\bar{3}m$). Fig. 2b and c show the annealing-temperature-dependent shift of the (311) peak, which first appeared at 650 °C. The peak position positively shifts from 35.4° to 35.8° between 650 °C and 800 °C, and the peak symmetry increases with the temperature, indicating the reduction of lattice distortion in HESOs crystal. Tiny diffraction peaks appeared at 37.25° and 43.28° when the synthesis temperature reached 800 °C, representing secondary phase (NiO PDF# 71-1179) formation at higher temperatures. Compared to that of the equimolar HESO,

similar diffraction patterns are found for binary, ternary, and quaternary samples in Fig. S1,† except that minor crystalline impurity (Fe_2O_3 and Co_3O_4) appearing on binary and quaternary because of the surplus precursors in the mixture.

The morphologies of the obtained HESOs were studied by SEM. Fig. S2d† showed the morphology of the as-obtained equimolar HESO, which consisted of small nanoparticles. Fig. S3a† shows the TEM image of the equimolar HESO. It is observed that the nanoparticles are faceted. The magnified TEM image (Fig. S3b†) shows distinct lattice fringes, with a measured lattice spacing of 0.481 nm, corresponding to the (111) facets. The (ADF)-STEM image and the mapping images are presented in Fig. S3c–i.† O, Fe, Ni, Co, Mn, and Zn elements are found to be homogeneously distributed in the nanoparticles.

From the synthesis process of the equimolar samples, we found that the five elements of Fe, Ni, Co, Mn, and Zn have good solubility in molten salts. The resultant chemical composition can be adjusted by the precursor ratio. Therefore, we also explored how the proportion of certain metal elements affects the catalytic activity in the OER. Here, we selected two AB_2O_4-type spinel oxides that have been studied for OER, $CoMn_2O_4$, and $NiFe_2O_4$ as the model system. In our approach, element A (Co and Ni) and element B (Mn and Fe) each account for approximately 33% of the atomic ratio. In comparison, approximately 33% of the remaining atomic ratio will be evenly distributed among the other three elements. In this way, CoMn-rich and NiFe-rich HESOs were successfully synthesized using the MSS method. The SEM-EDS data in Table S1† shows the atomic ratios of these samples closely corresponding to the precursor incorporation. Additionally, the ICP-MS data shown in Fig. S4† further confirm this consistency, indicating that the elemental molar ratios in the HESOs are largely derived from the precursors. The XRD patterns of the resulting HESOs in Fig. S5† show a spinel-type crystal structure. Meanwhile, the CoMn-rich and NiFe-rich HESOs show similar morphologies to the equimolar HESO according to the SEM (in Fig. 2d and S6†) and TEM (in Fig. 2e and S7†) observations. Fig. 2f illustrates clear atomic interplanar spacing of 0.24 nm, corresponding well to the adjacent (222) lattice fringes. The elemental mapping images of Fe, Ni, Co, Mn, Zn, and O in the non-equimolar HESOs verified the homogeneous mixing of each element (in Fig. 2g–m and S8†).

The electrocatalytic performances of the obtained oxide nanoparticles were measured in an alkaline condition (1.0 M KOH aqueous solution) under room temperature by LSV, where
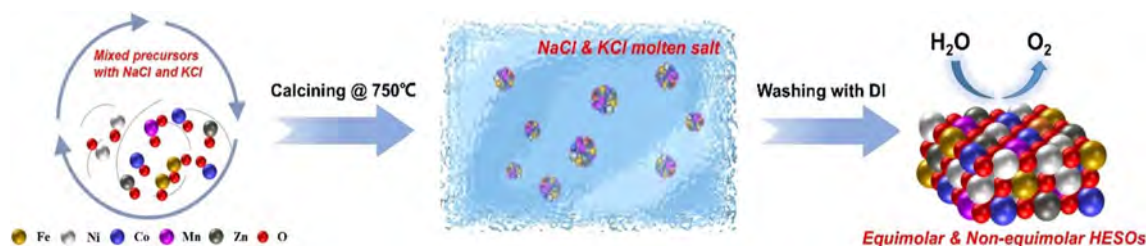

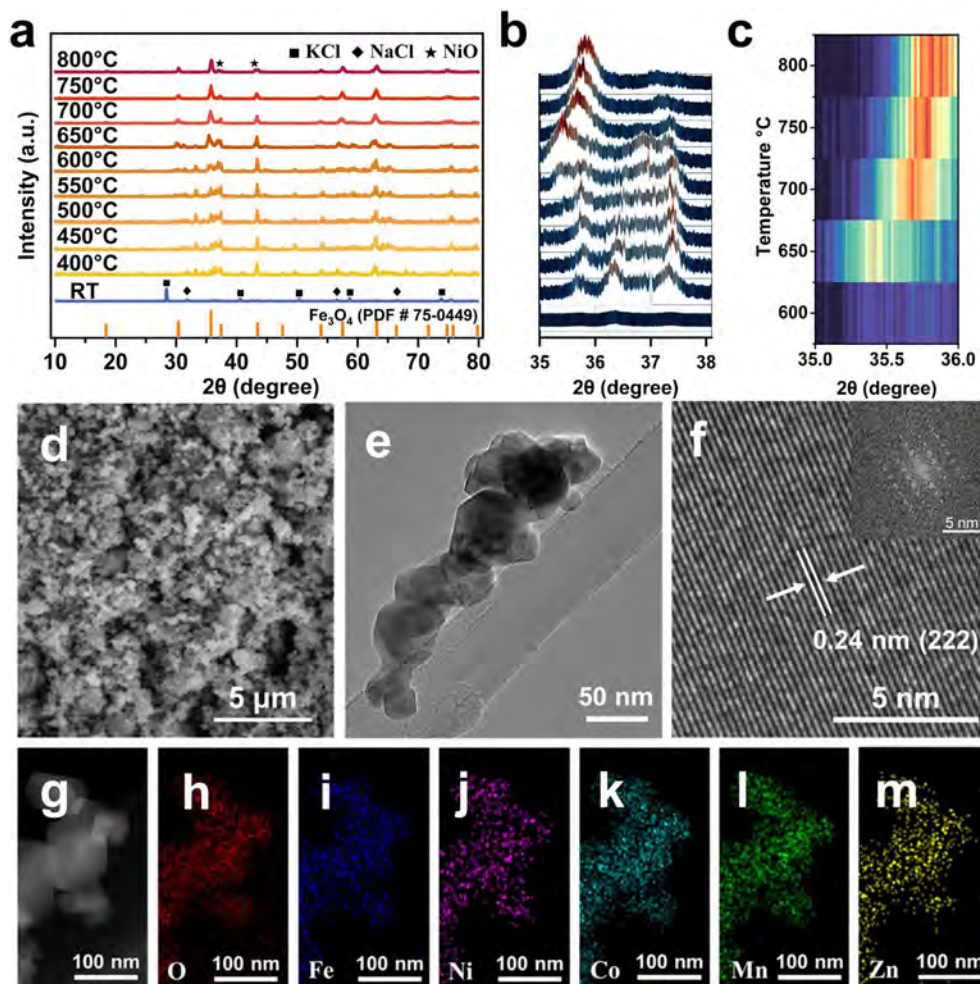Fig. 1 Schematic illustration of synthesis procedures of HESO by the MSS method.

13298 | *J. Mater. Chem. A*, 2025, 13, 13295–13304

This journal is © The Royal Society of Chemistry 2025

Fig. 2 (a) XRD pattern of equimolar HESO nanoparticles at different temperatures; (b) the corresponding (311) peak shift and (c) contour maps; microstructural characterization of CoMn-rich nanoparticles: (d) SEM image; (e) TEM image; (f) magnified image of a part of (e) with FFT; (g) annular dark-field (ADF)-STEM image and (h–m) EDS elemental mappings of O, Fe, Ni, Co, Mn, and Zn elements corresponding to (g).

the negative shifts of curves represented an increase in catalytic activity. Firstly, the OER performance of the equimolar HESO with different numbers of cations (hence different degrees of entropy) is compared. As shown in Fig. S9,† $(Ni_{0.2}Fe_{0.2}Co_{0.2}-Mn_{0.2}Zn_{0.2})_3O_4$ exhibits the lowest overpotential compared to its low-entropy counterparts due to the synergistic effects in HEOs. When comparing the OER performance among all three HESOs in Fig. 3a, the CoMn-rich HESO exhibited the best OER performance, achieving a benchmark current density of 10 mA cm^{-2} with an overpotential of only 330.1 mV much lower than equimolar HESO (359 mV) and NiFe-rich HESO (443.1 mV), and even lower than RuO_2 (341.6 mV). The Tafel slope plots were calculated from the corresponding polarization curves to assess the catalytic kinetics. The CoMn-rich HESO exhibits a lower Tafel slope (53.5 mV dec^{-1}) than those of the equimolar HESO (57.6 mV dec^{-1}), the NiFe-rich HESO (111.8 mV dec^{-1}) and the RuO_2 (151.8 mV dec^{-1}) (Fig. 3c). In this way, the CoMn-rich HESO demonstrates the most rapid kinetics for the OER, thereby minimizing the rate-determining step within the OER mechanism. The EIS was conducted to assess the charge-

transfer rate and the lowest responsive charge-transfer resistance (R_{ct}), which is conducive to enhancing OER (Fig. 3d). The R_{ct} for the CoMn-rich, RuO_2, equimolar, and NiFe-rich HESOs were 35.66 Ω, 37.93 Ω, 82.73 Ω, and 106.43 Ω, respectively. Therefore, it indicates that the CoMn-rich HESO possesses the fastest charge transfer ability, leading to the fastest OER kinetics. CV curves, illustrated in Fig. S10,† were obtained at different scan rates within the non-Faraday region. This approach allowed for the assessment of the C_{dl} for each electrocatalyst, as shown in Fig. 3e. The current shows a linear relationship with the scan rate, and its slope is C_{dl}. It is found that the CoMn-rich HESO possesses a much larger C_{dl} (0.6243 mF cm^{-2}) than the equimolar HESO (0.3048 mF cm^{-2}) and the NiFe-rich HESO (0.1309 mF cm^{-2}). The findings indicate that the CoMn-rich HESO has a large electrochemical active surface area and a high concentration of active sites, which enhances its electrocatalytic activity for OER. The OER FE was assessed by quantifying the experimentally generated O_2 and comparing it to the theoretical amount expected in a two-electrode cell with a 1 M KOH electrolyte. The observed O_2 production, as

This journal is © The Royal Society of Chemistry 2025

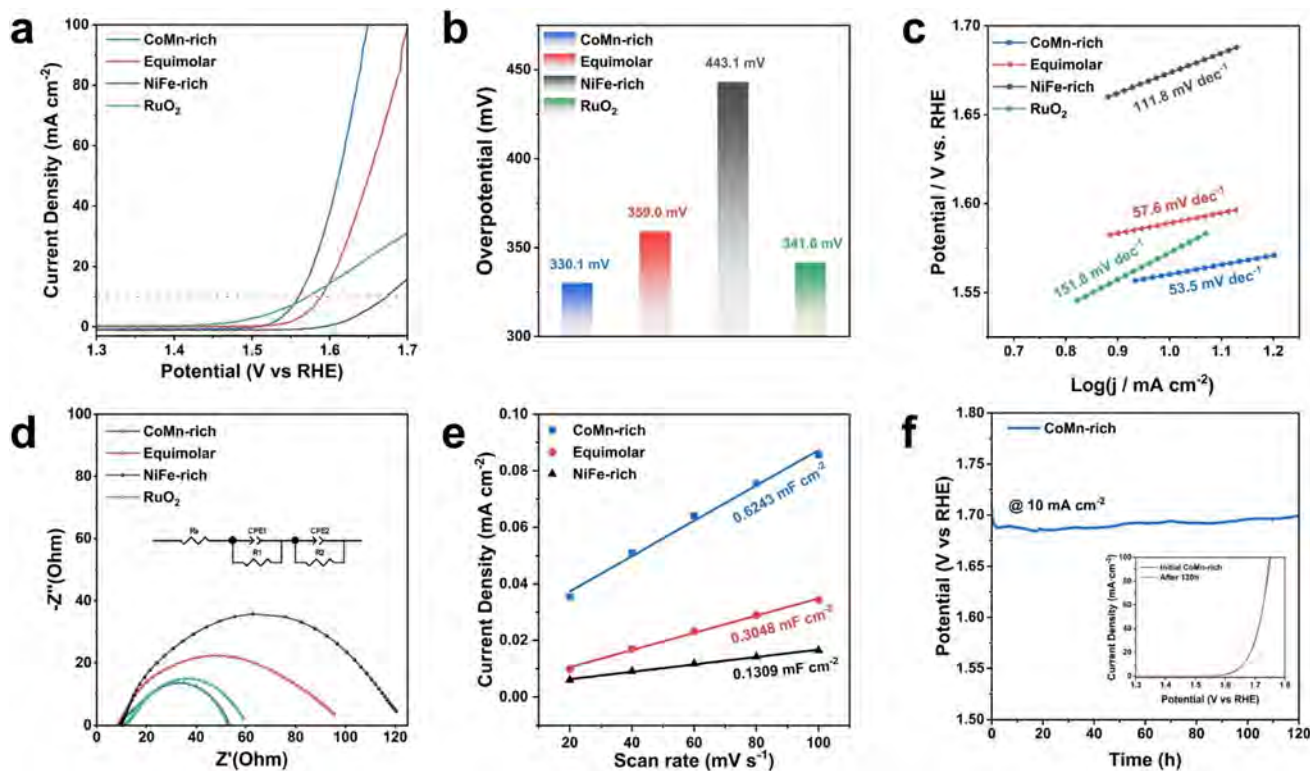*J. Mater. Chem. A*, 2025, **13**, 13295–13304 | **13299**

Fig. 3 Electrochemical characterizations of HEO in 1 M KOH solution. (a) LSV curves of three types of HESOs and RuO$_2$. (b) Overpotentials at 10 mA cm^{-2}. (c) Tafel slopes. (d) EIS with the corresponding equivalent circuit. (e) C_{dl} curves. (f) Stability test (insert: LSV curves of CoMn-rich before and after stability test).

illustrated in Fig. S11,† closely matches the predicted O$_2$ yield based on the current, demonstrating that the CoMn-rich catalyst achieves nearly 100% efficiency for O$_2$ generation in an alkaline environment. The TOF values for CoMn-rich, equimolar, and NiFe-rich catalysts are 0.0486 s^{-1}, 0.022 s^{-1} and 0.00314 s^{-1}, respectively. These results suggest that the CoMn-rich one exhibits the most rapid oxygen evolution at active sites. Moreover, the CoMn-rich HESO in Fig. 3f demonstrates good stability in the alkaline media, maintaining performance at 10 mA cm^{-2} for 120 hours without significant degradation. To better elucidate the catalyst's stability characteristics, XRD and SEM analyses, as shown in Fig. S12 and S13,† characterize the structure of the HESO after the CP test. The results indicate that the CoMn-rich HESO retains its original spinel-type structure, with no significant changes in morphology or crystallinity. Finally, a comprehensive comparison with several reported HEOs and spinel oxides is presented in Table S2.† The results indicate that CoMn-rich HESOs exhibit significantly enhanced OER catalytic performance compared to these reported materials. The superior catalytic activity of CoMn-rich underscores the importance of exploring HESO structures in developing advanced materials for electrochemical processes.

The electrochemical measurement results show that the CoMn-rich HESO exhibits the best electrocatalytic properties. XPS was employed to understand the surface chemical composition and valence states of the equimolar and non-equimolar HESOs to further explore the superior OER performance of the CoMn-rich HESO. The XPS spectra of each element (Fe, Ni, Co, Mn, Zn, and O) in as-synthesized HESO nanoparticles are displayed in Fig. 4a–f. The high-resolution Fe 2p (Fig. 4a) spectra of the three HESOs are illustrated in Fig. 4a. The peaks observed at 710.62 eV and 712.46 eV correspond to Fe 2p$_{3/2}$, while those at 723.94 eV and 725.41 eV are associated with Fe 2p$_{1/2}$.[31] The XPS spectrum of Ni 2p (Fig. 4b) is composed of two spin-orbit doublets; two peaks at 854.46 eV and 871.76 eV are related to Ni^{2+} 2p$_{3/2}$ and Ni^{2+} 2p$_{1/2}$. In comparison, the adjacent two peaks at 855.6 eV and 872.9 eV are attributed to Ni^{3+} 2p$_{3/2}$ and Ni^{3+} 2p$_{1/2}$.[51] As for Co 2p (Fig. 4c), one pair of doublets at 780.51 eV and 795.5 eV is assigned to Co^{3+}, and the other pair of doublets at 782.21 eV and 797.2 eV is attributed to Co^{2+}.[52] Besides, the first doublets at 642.25 eV and 653.76 eV are ascribed to Mn^{2+} 2p$_{3/2}$ and Mn^{2+} 2p$_{1/2}$ and the second at 643.93 eV and 655.37 eV are ascribed to Mn^{3+} 2p$_{3/2}$ and Mn^{3+} 2p$_{1/2}$ in Fig. 4d.[31] For the Zn 2p XPS spectrum (Fig. 4e), Zn^{2+} 2p$_{3/2}$ and Zn^{2+} 2p$_{1/2}$ are located at 1021.08 eV and 1044.17 eV.[53] These results reveal that Fe, Ni, Co, and Mn exhibit multi-valence states, while Zn is in a mono-valence state in these three HESOs.

To further investigate the surface conditions of the HESOs, the peak area ratios of Fe, Ni, Co, Mn, and Zn with different valence states are obtained and listed in Table S3.† It is observed that despite the composition difference in all three HESOs, the ratio of 2+ and 3+ ions of Ni and Mn are similar. Interestingly, the Fe^{2+} species is more dominant for the NiFe-rich HESO than the Fe^{3+} species. At the same time, the other elements have a similar 2+ : 3+ ion ratio, indicating the
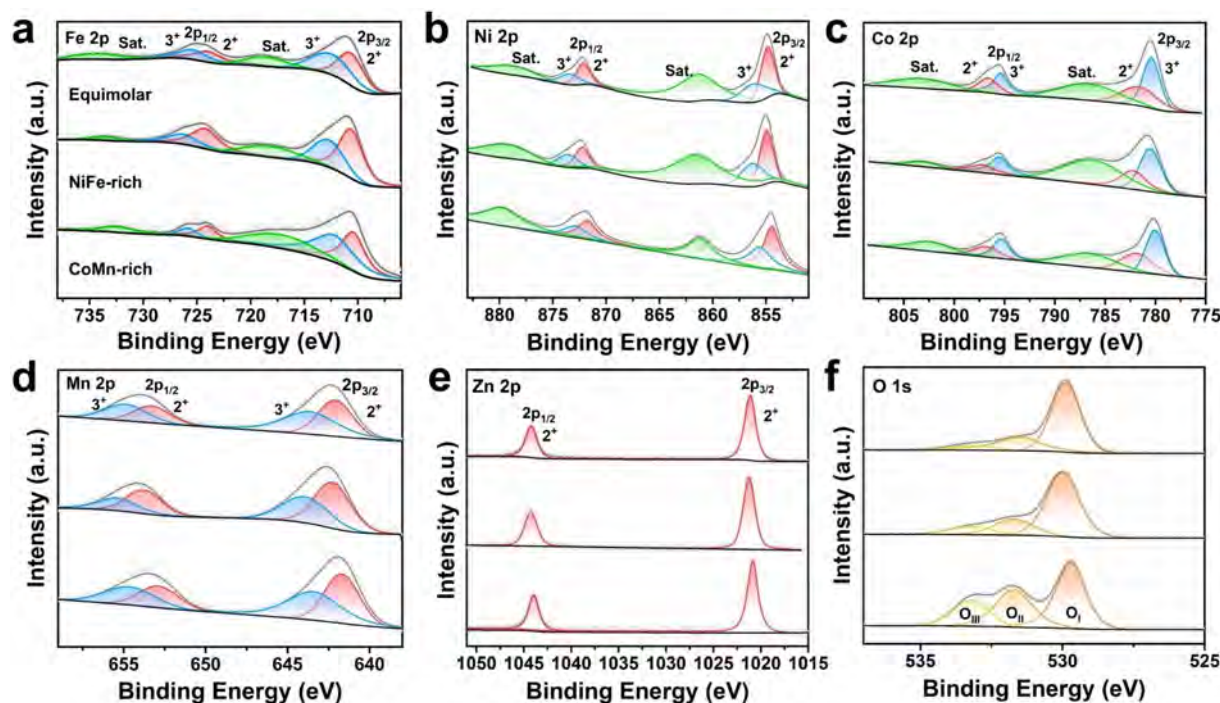
Fig. 4 High-resolution XPS spectra of the equimolar, the NiFe-rich, and the CoMn-rich samples: (a) Fe 2p, (b) Ni 2p, (c) Co 2p, (d) Mn 2p, (e) Zn 2p, and (f) O 1s.

enhanced amount of Ni and Fe content induces the reduction of Fe^{3+} ions. For the CoMn-rich HESO, the Co components are more oxidized and show a higher valence state (Co^{3+}). Although Ni, Fe, and Mn show a similar 2+ : 3+ ratio compared to the equimolar and NiFe-rich HESOs, the higher amount of Mn in CoMn-rich HESOs and its greater proportion of high-valence states may serve as an additional contributing factor to the improved OER performance. Higher valence state transition metal sites can enhance the reaction's kinetic and intrinsic activity. This enhancement occurs due to increased hole concentration in the d-band of oxidized metal species, which strengthens the covalency of metal–oxygen bonds and facilitates charge transfer.[54,55] Furthermore, the O 1s spectrum in Fig. 4f is deconvoluted into three peaks at 529.7, 531.8, and 533.1 eV (marked as O_I, O_{II}, and O_{III}), corresponding to the lattice oxygen, surface adsorbed oxygen species, and surface-adsorbed water, respectively. Here, the important role of O_{II} in catalysts should be noticeable since it has been reported to contribute to the adsorption capacity of oxygen-containing substances and enhance electrochemical performance.[56] Therefore, the content of O_{II} (Table S4†) is further calculated from the peak area ratio, revealing that the CoMn-rich HESO has the highest ratio of O_{II} (32.35%). The apparent higher O_{II} ratio manifests that the CoMn-rich HESO has stronger adsorption capacity on the surface. Besides, the contents of O_{III} in CoMn-rich HESO (21.27%) are also higher than equimolar HESO (6.34%) and NiFe-rich HESO (10.63%), as shown in Table S4,† indicating that the dissociation of O–H bonds and the formation of oxygen vacancies on its surface facilitates the electrocatalytic performance.[57] To study the dynamic changes in surface oxygen

species of the HESOs, Ar^+ sputtering at an energy of 4.86 kV was performed on the sample surface to track changes in oxygen species. As shown in Fig. S14 and Table S5,† the proportion of O_{III} in the three samples decreased to 0, while the ratios of O_I and O_{II} increased slightly but remained relatively unchanged overall. Moreover, the CoMn-rich sample still exhibits the highest proportion of O_{II} among all three HESO samples, indicating that its high O_{II} content is not solely a surface effect but also in the bulk.

To shed light on the reaction mechanism, XPS analyses are conducted on CoMn-rich after the CP test, as shown in Fig. S15.† According to the results of the XPS analysis, the binding energy of Zn 2p remains relatively unchanged, whereas the peaks of Co 2p, Mn 2p, Fe 2p, and Ni 2p shift towards higher binding energies. These shifts suggest the increase of high valence state elements after the OER, suggesting the active involvement of multiple metal species, with Co being the dominant species. Furthermore, the increased high valence elements on the material surface help to avoid additional changes while also strengthening the stability of materials.[58] Also, the concentration of O_{II} increases from 37.88% before the CP test to 43.48% after CP, as shown in the O 1s spectrum (Fig. S15f†), suggesting a potential lattice oxygen-mediated mechanism.[57]

The electronic structure of HESOs was investigated using DFT simulations to explore the enhancement of the electrocatalytic activity of OER. The most stable crystal bulk of the CoMn-rich, NiFe-rich, and equimolar HESOs, along with their atomic structures, are chosen from randomly sampled 400 different bulks (in Fig. S16†), where all Zn atoms are located on

This journal is © The Royal Society of Chemistry 2025

J. Mater. Chem. A, 2025, **13**, 13295–13304 | **13301**

the tetrahedral site and Fe, Ni, Co, and Mn atoms are located on both the tetrahedral and octahedral site. The (010) surface retains lower surface energy compared with the (111) and (110) in spinel-type cubic was cleaved from the optimized bulk structure of the equimolar, the CoMn-rich, and the NiFe-rich HESOs with layers of atoms. A slab model of the CoMn-rich, NiFe-rich, and equimolar HESOs with exposed (010) facet of spinel phase is constructed by Materials Studio,[59] as shown in Fig. 5a and S17† to further explore the intrinsic active site of these three HESOs. The OER process is then calculated with DFT to understand the contribution of each element in these HESOs. As shown in Fig. 5b and S18,† the reaction pathways with metal centers served as the catalytic active site go through four coordinated proton-electron transfer steps to generate oxygen. The energy diagram for metals (Fe, Ni, Co, and Mn) incorporates the adsorption energies of intermediates, including *OH, *O, and *OOH (Fig. S19a–c†). For the CoMn-rich HESO, the Co site exhibits the lowest energy barrier (2.69 eV) as compared to Fe (3.23 eV), Ni (3.71 eV), Mn (4.72 eV) in the rate-determining step, implying a high activity of Co site in OER process. In addition, the Co atoms in the equimolar sample display the lowest energy barrier (2.76 eV) relative to Mn (3.28 eV), Fe (4.63 eV), and Ni (8.60 eV). On the other hand, the Fe site of NiFe-rich shows the lowest energy barrier (2.88 eV) relative to Mn (4.02 eV), Ni (5.74 eV), and Co (6.96 eV). Thus, Co is considered the active site for CoMn-rich and the equimolar HESOs, while Fe of the NiFe-rich HESO dominates OER. The

energy diagrams of OER reaction pathways for the CoMn-rich, NiFe-rich, and equimolar HESOs with the corresponding reactive site are shown in Fig. 5c. For both non-equimolar HESOs, the third step showing the highest energy barrier is the potential determine step (PDS), which illustrates that the formation of *OOH is dynamically unfavorable. However, the first step in forming *OH species is the PDS in the equimolar HESO. The PDS overcomes an energy barrier of 2.69 eV, which is the lowest among these HESOs, indicating the enhanced catalytic performance of the CoMn-rich HESO in OER.

Meanwhile, the DOS for CoMn-rich, NiFe-rich, and equimolar HESOs was simulated to investigate the effect of the orbitals of the active center on the interactions between the adsorbate and catalyst. The DOS diagrams of three intermediates (*OH, *O, and *OOH) adsorbed on the catalyst surface with charge density difference mappings are shown in Fig. 5d, S20, and S21.† The synergistic effects among polymetallic atoms lead to varying overlaps between the d orbitals of the metal center and the p orbital of O across reaction steps. Notably, charge density difference maps reveal electron transfer between these metallic elements, indicating electronic coupling. Significant charge transfer occurs not only on the Co directly beneath *OH, *O, and *OOH but also on the adjacent and subsurface Mn and Co atoms, as shown in Fig. S22.† This suggests that the synergistic effect of Co and Mn significantly influences the adsorption of these functional groups and, consequently, the OER activity. In Fig. S19.† for the CoMn-rich HESO, the energy
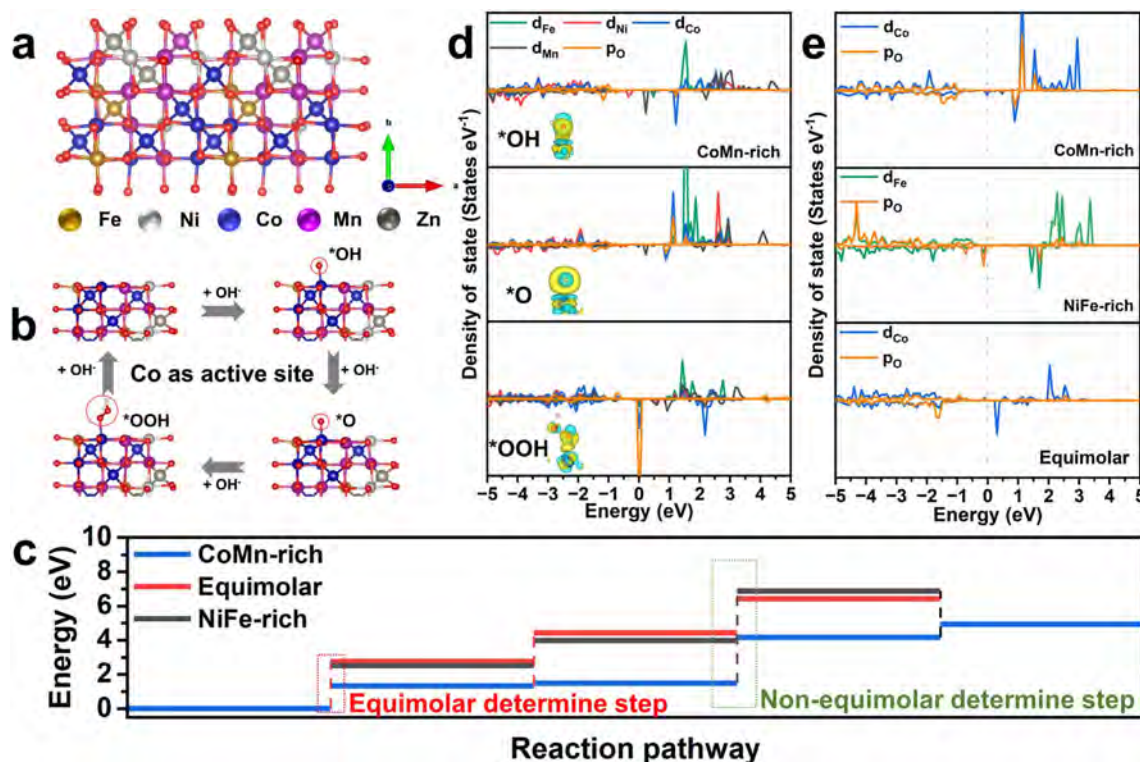

Fig. 5 (a) Top view of the stable (010)-plane structure of the CoMn-rich HESO. (b) The reaction pathway at the cobalt metal site for OER. (c) OER energy diagram optimal for each HESOs. (d) Spin-resolved DOS and charge density difference maps of CoMn-rich at *OH, *O, and *OOH adsorption step (the yellow and blue regions represent charge accumulation and depletion, respectively). (e) DOS of the *O adsorption step on the different HESO surfaces.

13302 | J. Mater. Chem. A, 2025, **13**, 13295–13304

This journal is © The Royal Society of Chemistry 2025

change between the initial and *O states is the lowest among the three HESO structures, at only 1.7 eV. In contrast, the energy changes for the adsorption of O at the Fe site in the NiFe-rich HESO and at the Co site in the equimolar HESO are 4 and 4.2 eV, respectively. Additionally, Fig. 5e shows that the bonding interaction between the Co site and the O atom in the CoMn-rich HESO is the strongest among the three HESOs. Stronger bonding interactions stabilize the adsorbed O atom on the surface. The overlap between d orbitals of the transition metal center and p orbitals of *O is likely attributed to the synergistic effects among the polymetallic atoms in the HESO. In the charge density difference maps, an apparent charge transfer phenomenon can be clearly visualized between the adsorbate and catalyst, indicating that the formation of electronic coupling on the surface facilitates the improvement of OER performance. The d orbitals of the metal active sites overlap with the p orbitals of O, as shown in Fig. 5e, indicating the formation of stronger interactions at the catalyst surface, suggesting that the electron transfer should be faster in the CoMn-rich HESO, which agrees with the previous analysis of higher efficiency of electrocatalysis.

4. Conclusion

In conclusion, we have successfully synthesized the HESO nanoparticles using the MSS method. The obtained HESOs exhibit an even distribution of metal ions, ensuring the effective mixing of different elements. The HESOs also demonstrate good crystallinity. Regarding OER performance, when compared to spinel oxides with lower entropy obtained by the same method, significant improvement in the catalytic performance of HESOs was shown, characterized by lower over-potential and smaller Tafel slope values. This underscores the potential advantages of HESOs over traditional low-entropy oxide. Furthermore, by adjusting the ratio of different precursors, we synthesized CoMn-rich HESO nanoparticles that exhibit the best performance among all HESO samples, offering a viable approach for enhancing catalytic activity. The enhanced performance is attributed to the synergistic effect of Co and Mn with high valence states, which optimizes the electronic structure to facilitate the charge transfer. Additionally, advanced spectral analysis combined with DFT indicates that strong d–p orbital hybridization in CoMn-rich HESO promotes efficient electron transfer, attributed to high valence states. This interaction significantly boosts oxygen species adsorption on the surface, leading to enhanced catalytic performance in the OER. These results underscore the material's promise as a highly effective electrocatalyst. In summary, we have demonstrated a straightforward approach to improve the OER performance of HESOs. These results provide insights for further enhancing the performance of these HESOs in OER applications.

Data availability

The data supporting this article have been included as part of the ESI.†

Author contributions

D. S. led the work and wrote the manuscript. D. S. and S. Y. designed the experiments. D. S. and X. L. synthesized the samples and structural characterization. D. S., X. L., and Q. Q. performed the electrochemical measurements. Y. W., D. S., and Y. T. conducted DFT calculations. X. L., X. L., S. I., and H. S. performed the parts of characterizations. D. S. and X. L. analyzed the data. S. Y., T. Y., and J. C. H. directed this work. All authors discussed and revised the manuscript.

Conflicts of interest

The authors declare no competing financial interests.

Acknowledgements

References

1 N.-T. Suen, S.-F. Hung, Q. Quan, N. Zhang, Y.-J. Xu and H. M. Chen, *Chem. Soc. Rev.*, 2017, **46**, 337–365.
2 J. S. Kim, B. Kim, H. Kim and K. Kang, *Adv. Energy Mater.*, 2018, **8**, 1702774.
3 W. Lubitz and W. Tumas, *Chem. Rev.*, 2007, **107**, 3900–3903.
4 J. A. Turner, *Science*, 2004, **305**, 972–974.
5 H. Ahmad, S. Kamarudin, L. J. Minggu and M. Kassim, *Renewable Sustainable Energy Rev.*, 2015, **43**, 599–610.
6 J. Chi and H. Yu, *Chin. J. Catal.*, 2018, **39**, 390–394.
7 S. Wang, A. Lu and C.-J. Zhong, *Nano Convergence*, 2021, **8**, 4.
8 Y. Cheng, *Prog. Nat. Sci.:Mater. Int.*, 2015, **25**, 545–553.
9 Z. P. Wu, X. F. Lu, S. Q. Zang and X. W. Lou, *Adv. Funct. Mater.*, 2020, **30**, 1910274.
10 Q. Pan and L. Wang, *J. Power Sources*, 2021, **485**, 229335.
11 H. Wu, C. Feng, L. Zhang, J. Zhang and D. P. Wilkinson, *Electrochem. Energy Rev.*, 2021, **4**, 473–507.
12 B. Tamilarasi, K. Jithul and J. Pandey, *Int. J. Hydrogen Energy*, 2024, **58**, 556–582.
13 X.-F. Lu, L.-F. Gu, J.-W. Wang, J.-X. Wu, P.-Q. Liao and G.-R. Li, *Adv. Mater.*, 2016, **29**, 1604437.
14 S. L. Zhang, B. Y. Guan, X. F. Lu, S. Xi, Y. Du and X. W. Lou, *Adv. Mater.*, 2020, **32**, 2002235.
15 V. Vij, S. Sultan, A. M. Harzandi, A. Meena, J. N. Tiwari, W.-G. Lee, T. Yoon and K. S. Kim, *ACS Catal.*, 2017, 7, 7196–7225.

This journal is © The Royal Society of Chemistry 2025

J. Mater. Chem. A, 2025, **13**, 13295–13304 | **13303**

16 J. W. Yeh, S. K. Chen, S. J. Lin, J. Y. Gan, T. S. Chin, T. T. Shun, C. H. Tsau and S. Y. Chang, *Adv. Eng. Mater.*, 2004, **6**, 299–303.

17 C. Oses, C. Toher and S. Curtarolo, *Nat. Rev. Mater.*, 2020, **5**, 295–309.

18 L. He, H. Kang, G. Hou, X. Qiao, X. Jia, W. Qin and X. Wu, *Chem. Eng. J.*, 2023, **460**, 141675.

19 Y. Mei, Y. Feng, C. Zhang, Y. Zhang, Q. Qi and J. Hu, *ACS Catal.*, 2022, **12**, 10808–10817.

20 T. X. Nguyen, Y. H. Su, C. C. Lin and J. M. Ting, *Adv. Funct. Mater.*, 2021, **31**, 2106229.

21 J. Chang, G. Wang, C. Li, Y. He, Y. Zhu, W. Zhang, M. Sajid, A. Kara, M. Gu and Y. Yang, *Joule*, 2023, **7**, 587–602.

22 Y. Xu, X. Xu and L. Bi, *J. Adv. Ceram.*, 2022, **11**, 794–804.

23 B. Yang, Y. Zhang, H. Pan, W. Si, Q. Zhang, Z. Shen, Y. Yu, S. Lan, F. Meng and Y. Liu, *Nat. Mater.*, 2022, **21**, 1074–1080.

24 A. Amiri and R. Shahbazian-Yassar, *J. Mater. Chem. A*, 2021, **9**, 782–823.

25 Y. Ma, Y. Ma, Q. Wang, S. Schweidler, M. Botros, T. Fu, H. Hahn, T. Brezesinski and B. Breitung, *Energy Environ. Sci.*, 2021, **14**, 2883–2905.

26 Y. Sun and S. Dai, *Sci. Adv.*, 2021, **7**, eabg1600.

27 S. Schweidler, M. Botros, F. Strauss, Q. Wang, Y. Ma, L. Velasco, G. Cadilha Marques, A. Sarkar, C. Kübel and H. Hahn, *Nat. Rev. Mater.*, 2024, **9**, 266–281.

28 M. S. Lal and R. Sundara, *ACS Appl. Mater. Interfaces*, 2019, **11**, 30846–30857.

29 S. Jiang, Y. Yu, H. He, Z. Wang, R. Zheng, H. Sun, Y. Liu and D. Wang, *Small*, 2024, 2310786.

30 Y. Zhang, W. Dai, P. Zhang, T. Lu and Y. Pan, *J. Alloys Compd.*, 2021, **868**, 159064.

31 D. Wang, Z. Liu, S. Du, Y. Zhang, H. Li, Z. Xiao, W. Chen, R. Chen, Y. Wang and Y. Zou, *J. Mater. Chem. A*, 2019, **7**, 24211–24216.

32 T. X. Nguyen, Y. C. Liao, C. C. Lin, Y. H. Su and J. M. Ting, *Adv. Funct. Mater.*, 2021, **31**, 2101632.

33 F. Otto, Y. Yang, H. Bei and E. P. George, *Acta Mater.*, 2013, **61**, 2628–2638.

34 Y. Zhang, Y. J. Zhou, J. P. Lin, G. L. Chen and P. K. Liaw, *Adv. Eng. Mater.*, 2008, **10**, 534–538.

35 Y. Zhang, T. T. Zuo, Z. Tang, M. C. Gao, K. A. Dahmen, P. K. Liaw and Z. P. Lu, *Prog. Mater. Sci.*, 2014, **61**, 1–93.

36 K. Gu, D. Wang, C. Xie, T. Wang, G. Huang, Y. Liu, Y. Zou, L. Tao and S. Wang, *Angew. Chem.*, 2021, **133**, 20415–20420.

37 S. K. Gupta and Y. Mao, *Prog. Mater. Sci.*, 2021, **117**, 100734.

38 Y. Mao, T. J. Park, F. Zhang, H. Zhou and S. S. Wong, *Small*, 2007, **3**, 1122–1139.

39 T. Kimura, *Advances in Ceramics-Synthesis and Characterization, Processing and Specific Applications*, 2011, pp. 75–100.

40 X. Liu, N. Fechler and M. Antonietti, *Chem. Soc. Rev.*, 2013, **42**, 8237–8265.

41 J. P. Zuniga, M. Abdou, S. K. Gupta and Y. Mao, *J. Visualized Exp.*, 2018, **140**, 58482.

42 T. Xue, X. Liu, H. Lei, H. Dai, Z. Huang and H. Zhang, *Ceram. Int.*, 2024, **50**, 18294–18302.

43 G. Kresse and J. Furthmüller, *Comput. Mater. Sci.*, 1996, **6**, 15–50.

44 G. Kresse and J. Furthmüller, *Phys. Rev. B:Condens. Matter Mater. Phys.*, 1996, **54**, 11169.

45 J. P. Perdew, K. Burke and M. Ernzerhof, *Phys. Rev. Lett.*, 1996, **77**, 3865.

46 C. E. Calderon, J. J. Plata, C. Toher, C. Oses, O. Levy, M. Fornari, A. Natan, M. J. Mehl, G. Hart and M. B. Nardelli, *Comput. Mater. Sci.*, 2015, **108**, 233–238.

47 G. Kresse and D. Joubert, *Phys. Rev. B:Condens. Matter Mater. Phys.*, 1999, **59**, 1758.

48 S. Grimme, S. Ehrlich and L. Goerigk, *J. Comput. Chem.*, 2011, **32**, 1456–1465.

49 Q. Liang, G. Brocks and A. Bieberle-Hütter, *J. Phys.: Energy*, 2021, **3**, 026001.

50 V. A. Mints, K. L. Svane, J. Rossmeisl and M. Arenz, *ACS Catal.*, 2024, **14**, 6936–6944.

51 J. Yan, L. Chen and X. Liang, *Sci. Bull.*, 2019, **64**, 158–165.

52 Z. Liu, H. Tan, D. Liu, X. Liu, J. Xin, J. Xie, M. Zhao, L. Song, L. Dai and H. Liu, *Adv. Sci.*, 2019, **6**, 1801829.

53 K. Miao, W. Jiang, Z. Chen, Y. Luo, D. Xiang, C. Wang and X. Kang, *Adv. Mater.*, 2024, **36**, 2308490.

54 H. Wang, T. Zhai, Y. Wu, T. Zhou, B. Zhou, C. Shang and Z. Guo, *Adv. Sci.*, 2023, **10**, 2301706.

55 M. Cui, X. Ding, X. Huang, Z. Shen, T.-L. Lee, F. E. Oropeza, J. P. Hofmann, E. J. Hensen and K. H. Zhang, *Chem. Mater.*, 2019, **31**, 7618–7625.

56 T. J. Frankcombe and Y. Liu, *Chem. Mater.*, 2023, **35**, 5468–5474.

57 N. Zhang, X. Feng, D. Rao, X. Deng, L. Cai, B. Qiu, R. Long, Y. Xiong, Y. Lu and Y. Chai, *Nat. Commun.*, 2020, **11**, 4066.

58 S. Jiang, K. Tian, X. Li, C. Duan, D. Wang, Z. Wang, H. Sun, R. Zheng and Y. Liu, *J. Colloid Interface Sci.*, 2022, **606**, 635–644.

59 BIOVIA., *Dassault Systems, Materials Studio 2022*, San Diego, CA, USA, 2022.